Nanotechnology

PAPER

Effects of cold atmospheric plasma treatment on the morphological and optical properties of plasmonic silver nanoparticles

To cite this article: Apurva Sonawane *et al* 2020 *Nanotechnology* **31** 365706

IOP Publishing Nanotechnology
Nanotechnology **31** (2020) 365706 (11pp) https://doi.org/10.1088/1361-6528/ab9788

Effects of cold atmospheric plasma treatment on the morphological and optical properties of plasmonic silver nanoparticles

Apurva Sonawane, Mubarak A Mujawar and Shekhar Bhansali

Department of Electrical and Computer Engineering, Florida International University, Miami, FL 33174, United States of America

E-mail: asona003@fiu.edu, mubarak.mujawar@fiu.edu and shekhar.bhansali@fiu.edu

Received 9 October 2019, revised 12 May 2020
Accepted for publication 28 May 2020
Published 24 June 2020

Abstract

The use of plasma processes in nanomaterial synthesis is limited by a lack of understanding of the effects of plasma treatment on the morphology and other properties. Here, we studied the effects of atmospheric plasma treatment on the morphology and optical properties of Ag nanoparticles. The Ag nanoparticles were deposited on substrates by injecting an aerosol into flowing argon gas and then treated with a low-temperature atmospheric plasma jet. After plasma treatment, the mean Ag nanoparticle diameter reduced to an average of 5 nm, which was accompanied by a blue shift of ~70 nm in the peak of the surface plasmon resonance; these results are similar to those obtained by thermal treatment at elevated temperatures. The reduction in nanoparticle size is explained by the redox reaction that occurs on the nanoparticle surface, which is evident from the presence of AgO and Ag_2O Raman peaks in the treated sample. The surface charge changed as a result of plasma treatment, as indicated by a large change in the zeta potential from $+25.1 \pm 4$ mV for the untreated sample to -25.9 ± 6 mV after 15 min of plasma treatment. Surface-enhanced Raman spectroscopy of the plasma-treated films was carried out with the fluorescent dye Rhodamine 6 G, which showed a ~120-fold enhancement in the signal intensity relative to the untreated substrates. We, therefore, conclude that cold-plasma treatment modified the surface morphology of the Ag nanoparticles, thereby enhancing their optical properties. This technique could be applied to a wide range of nanoparticle systems used in biosensing applications.

Supplementary material for this article is available online

Keywords: cold atmospheric plasma, surface-enhanced raman spectroscopy, surface plasmon resonance, silver nanoparticles, zeta potential

(Some figures may appear in colour only in the online journal)

1. Introduction

Plasmonic materials are vital for applications such as molecular-level biosensing and nanoscale electronics[1]. Plasmonic nanostructures, such as silver (Ag) and gold nanoparticles, enable amplification of the scattered signal by electromagnetic and chemical enhancement [2–5]. The morphology of metal nanoparticles (NPs) defines their plasmonic response, which can be altered by various techniques, including thermal annealing [6,7]. The thermal annealing [8–10] of NP films leads to a change in the mean NP diameter owing to agglomeration, creating an observable red or blue shift in the

1361-6528/20/365706+11$33.00

surface plasmon resonance (SPR). Ag NPs are an ideal candidate for optical applications [11,12] because of their high extinction coefficient, their tunable optical properties through their size and shape, and the SPR in the UV–visible region. These properties have been exploited in applications such as solar energy harvesting, light-emitting diodes, printed optoelectronic devices, and surface-enhanced Raman scattering (SERS) [13]. Ag NPs tend to form a natural oxide layer on their surface, which affects the symmetry of the electro-dissolution in electrochemical reactions, SPR and SERS [[14]. The symmetrical partial surface oxidation is acceptable for maintaining the shape of Ag NPs and their optical response [14].

The state-of-the-art techniques to control the NP size involve thermal annealing, which is not always desirable because it is limited to static, rigid surfaces and is not suitable for applications where non-planar, conformal, and flexible polymer substrates are required. Selective laser sintering of NPs can be used for processing polymer substrates; however, it is challenging to control the laser beam [15]. Plasma-assisted synthesis of NPs has emerged as an important research area of material science and nanotechnology [16]. Moreover, the plasma synthesis processes used to control NP size are highly complex [17]. Here, we propose a novel and simple approach of cold atmospheric plasma (CAP) treatment to provide energy to the Ag NP substrate, similar to that provided in thermal annealing but at room temperature. We deposited Ag NPs on substrates by injecting aerosol in flowing argon gas and then treated them with a low-temperature atmospheric plasma jet. The aerosolized NP deposition and plasma set-up are derived from our previous work [18] and that of Dey *et al* [19]. with a few modifications. The plasma technique used by Khan *et al* [20]. involves pulsed laser deposition and comparatively complex experimental assembly. By contrast, our set-up contains a simple nebulizer to create an aerosol of NPs for the deposition.

In this work, we observed a size reduction of Ag NPs after surface plasma treatment due to symmetric partial oxidation. The blue shift in the SPR signal was consistent with Mie theory; that is, the SPR absorbance peak was a function of the particle concentration and radius [21]. As-deposited films were used as the SERS substrate to detect R6 G peaks to characterize the optical properties. The SERS signal intensity from the plasma-treated substrate was ∼120 times higher than that of the untreated substrate. We attributed this enhancement to the size reduction, hot-spot formation, surface electron excitation, and increased surface roughness after plasma treatment. Plasma treatment also led to a substantial change in the effective electric charge on the Ag NPs surface, which we quantified using zeta potential measurements. The morphological changes of the Ag NPs are explained by a redox reaction induced by the high energy and high concentration of reactive species in the CAP environment.

2. Experimental methods

2.1. Aerosolized deposition and argon plasma assembly

Figure 1 shows the experimental set-ups used for Ag NP deposition (figures 1(a) and (b)) and for plasma treatment (figures 1(c) and (d)). For Ag NP deposition, an ultrasonic nebulizer was used to create an aerosol of the NP solution. The nebulizer was connected to a quartz tube to provide a desired path to the aerosol. The ultrasonic nebulizer was modified to have one inlet for Argon (Ar) gas and one outlet, which connected to the quartz tube, with an outer diameter of 6 mm and an inner diameter of 3 mm. A glass capillary with a 1-mm inner diameter was inserted into the quartz tube (Technical Glass Products, Ohio). Another Ar inlet was connected to the midway point of the quartz tube and was controlled by a mass flow controller (MFC). Teflon tape (Everflow Supplies) was used as a moisture blocker between the quartz tube and glass capillary (placed in front of the MFC outlet) to absorb the excess moisture created from the aerosol in the path before deposition.

To generate the plasma (figures 1(c) and (d)), a high-voltage supply (variable output of 1–20 kV; variable frequency of 20–60 kHz; current of 20–30 mA) was connected to two electrodes made from copper rings on the quartz tube. These tubular copper electrodes were placed 1 cm apart. The MFC-controlled Ar gas flow was supplied to the quartz tube to produce a stable Ar cold plasma. The Ar flow rate was set using a gas flow controller at 2 l min^{-1}. An external power supply was used to deliver sinusoidal power (∼10 kV, ∼30 kHz) to the electrodes. The high-voltage supply was turned on, and the impedance was adjusted in such a way that the voltage and variable frequency reached a point where the downstream plasma became stable. The voltage supply and gas flow were turned off after treatment.

Branched Polyethylenimine (BPEI)-functionalized Ag NPs of an average size of 10 nm were purchased from Sigma-Aldrich and used to make a 0.02 mg ml^{-1} solution in deionized water. The solution was poured into the nebulizer to create the aerosol. The aerosol was carried upwards by an Ar gas stream of ∼15 SCCM, which was supplied to the inlet of the nebulizer along the path through the quartz tube and the capillary. The Ar gas supplied to the midway of the quartz tube regulated the flow of the NPs for film deposition as required. The concentrated Ag NPs were carried through the capillary and were deposited on the quartz slides for SPR detection, on silicon for scanning electron microscopy (SEM), and SERS characterization, and on copper grids for transmission electron microscopy (TEM).

2.2. Plasma characterization

The optical emission spectra was recorded for the Ar gas CAP, as shown in figure 2. An optical emission spectrometer (Ocean Optics, HR2000 + ES) was used to obtain the intensity counts for the downstream plasma [22]. The intensities for the Ar transitions were also measured [23]. Using the ratio method [24], the relative intensities were plotted against relative higher-level energies for the respective transitions, as shown in the inset of figure 2; the relationship is given in equation (1) [25]:

$$\ln\left(\frac{I_1}{I_2}\right) = -\frac{E_1 - E_2}{kT} + \ln\left(\frac{A_1 g_2 \lambda_2}{A_2 g_2 \lambda_1}\right) \tag{1}$$

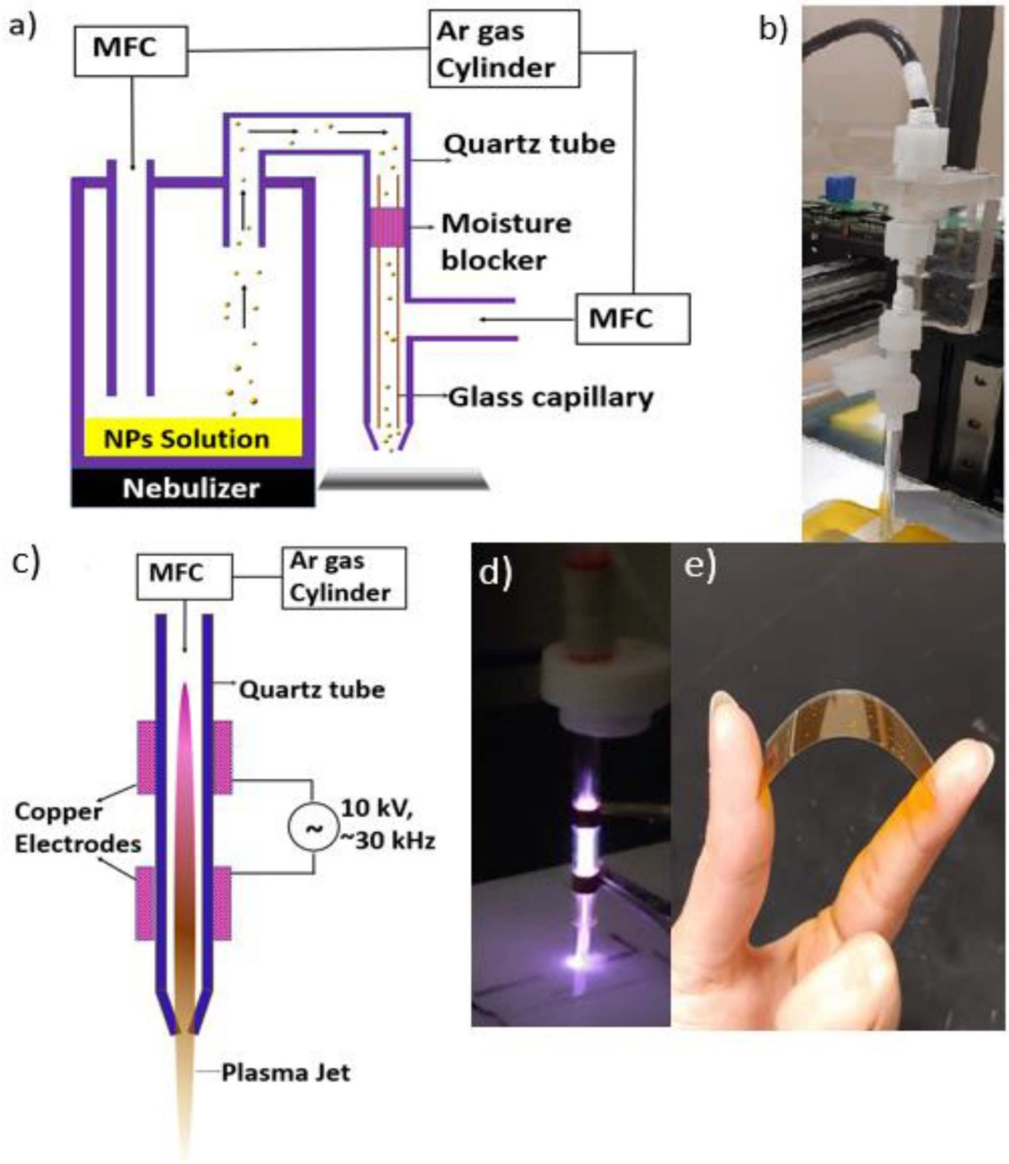

Figure 1. (a) Schematic illustration and (b) photograph of the experimental set-up for the deposition of Ag NPs on the substrate. (c) Schematic illustration and (d) photograph of the experimental set-up of the cold plasma unit. (e) Ag NPs deposited on a flexible polyimide film.

where A is the transition probability, g is the statistical weight of the electron, λ *i*s the wavelength associated with the transition, E is the higher-level energy for the transition, k is the Boltzmann constant, and T is electron temperature. To validate the above result, the relationship between the relative intensities and relative energies was plotted. The slope of the fitted plot was calculated, as shown in the inset of figure 2, and the electron temperature was found to be $T = 1.08$ eV. Using the Saha–Boltzmann method [26,27], the electron density, n_e, was calculated as:

$$n_e = 6.04x10^{21} x\frac{I_1}{I_2} x(T)^{\frac{3}{2}} e\left(\frac{xz - E_1 - E_2}{kT}\right) \quad (2)$$

where $\left(2\pi me\frac{K}{h^3}\right)^{\frac{3}{2}} = 6.04 \times 10^{21}$, and xz is the ionization potential of Ar (assumed to be 15 eV).

The electron density, $n_e = 1.9x10^{11}$ cm^{-3} is the number of electrons that were energized and excited into an ionized state.

2.3. *Plasma treatment and thermal annealing of NPs*

Samples for SPR were prepared by depositing Ag NPs on quartz slides followed by plasma treatment for 5, 10, or 15 min. For comparison between the plasma-treated and thermally annealed substrates, sets of as-deposited slides were annealed using rapid thermal processing (RTP) for the same duration at 250 and 400 °C in an Ar/O_2 environment. The thermal energy for the gas at 400 °C was 0.058 eV, which was obtained from the temperature of the gas used in RTP. SPR signals were measured for all samples using a UV–visible spectrometer (Thermo Fisher, Evolution 300).

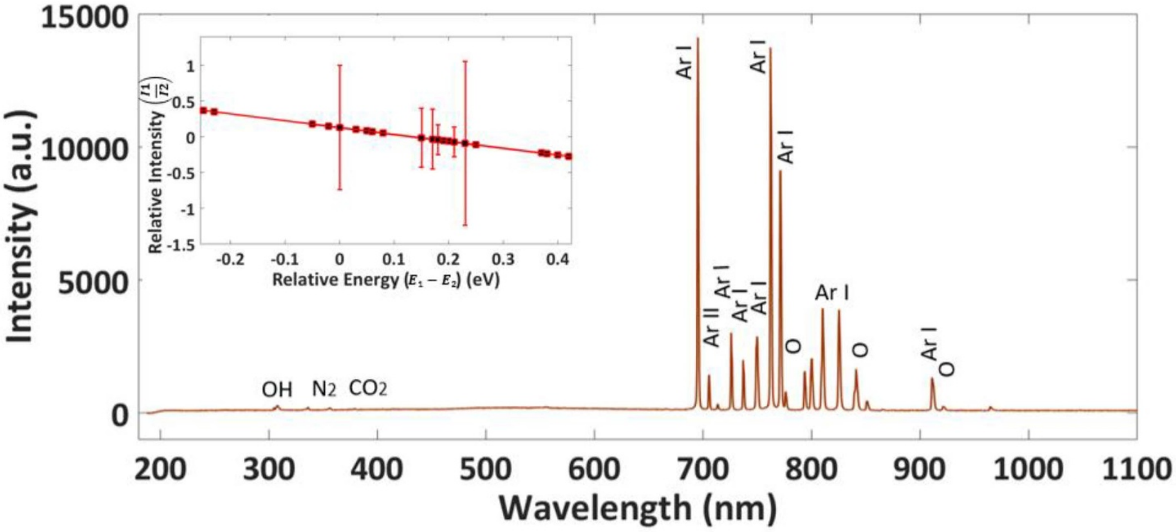

Figure 2. Optical emission spectra for Ar plasma. Inset: relative intensity of the ArI and ArII transitions with respect to the relative higher-energy level.

2.4. *Surface charge measurements*

The electric charge on the Ag NP surface after plasma treatment was analyzed by performing zeta potential measurements using a particle zetasizer (Malvern Instruments). AgNP dispersion was used to deposit on the quartz slides and then was treated with the plasma. Measurements were made using this dispersion in capillary zeta cells. The zeta potential was recorded for the suspension immediately after the treatment. The readings were taken for 15 runs and were averaged for five different samples.

2.5. *Surface-enhanced Raman spectroscopy*

Ag NPs were deposited on silicon substrates, and the SERS signal for R6 G was measured with and without plasma treatment. R6 G (Sigma Aldrich) was diluted to 5 μM and placed directly on the untreated and treated Ag NP films. A 10 μl probe solution was used to create a drop on the substrates, which was spread into the circle with a 4 mm diameter. The SERS signals of both the samples were recorded using a LabRAM HR spectrometer. The intensities were recorded at 30 selected points and then averaged. The spectral position was calibrated at the 520.5 cm^{-1} peak of Si/SiO$_2$, and signals were recorded at a 532 nm excitation wavelength with a diameter of the region under the laser beam of 5 μm. Gaussian–Lorentzian peak detection was used after subtracting the noise from the signal in 15 acquisitions. To calculate the enhancement factor, the peak intensities of the R6 G directly on the bare silicon substrate were detected after spreading it in a 4 mm-diameter circle and letting it dry. The EF for the recorded signals was calculated based on the methods used in Meyer *et al* [28]. and Li *et al* [29].

2.6. *Imaging*

The aerosolized Ag NPs were deposited with thermal and plasma treatment onto silicon substrates for SEM imaging (JOEL, SEM 7000 l) at an operating voltage of 20 kV and with a 9 μA probe current. The SEM images were processed using ImageJ software to obtain the Feret diameter distribution of the untreated and treated Ag NPs. The TEM images of the Ag NPs were captured using a Philips CM200 TEM at a 200 kV excitation voltage. Atomic force microscopy (AFM) images were recorded for samples prepared on silicon substrates using AFM WORKSHOP TT, and the results were processed using Gwyddion software tools. The surface roughness and texture of the untreated and plasma-treated samples were plotted.

3. Results and discussion

3.1. *Surface plasmon resonance*

The SPR absorption peaks of the untreated and thermally or plasma-treated Ag NPs films deposited on quartz substrates are shown in figures 3(a)–(c). The SPR peak of the untreated substrates was observed at 426 nm, which was blue-shifted to 415, 393, and 361 nm, after plasma treatment for 5, 10, and 15 min, respectively. Thermal annealing resulted in a blue shift of 7, 17, and 25 nm at 250 °C, and 9, 28, and 45 nm at 400 °C at 5, 10, and 15 min, respectively. After 15 min, no significant peak shift was observed for thermal annealing. Moreover, the strength of the SPR absorbance was reduced for the treated samples. An almost linear plot of the blue shift after plasma or thermal treatment is shown in figure 3(d), where the plasma treatment resulted in a similar resonance response to thermal annealing. From figure 3(d), we note that there was a larger shift in the SPR peak for plasma treatment than for thermal annealing for the same duration of the treatment.

The blue shift and the reduced intensity of the SPR peak in figure 3 suggest that plasma treatment reduced the size of the NPs and increased the distance between adjacent particles [30,31]. Because of the size reduction, the surface-to-volume

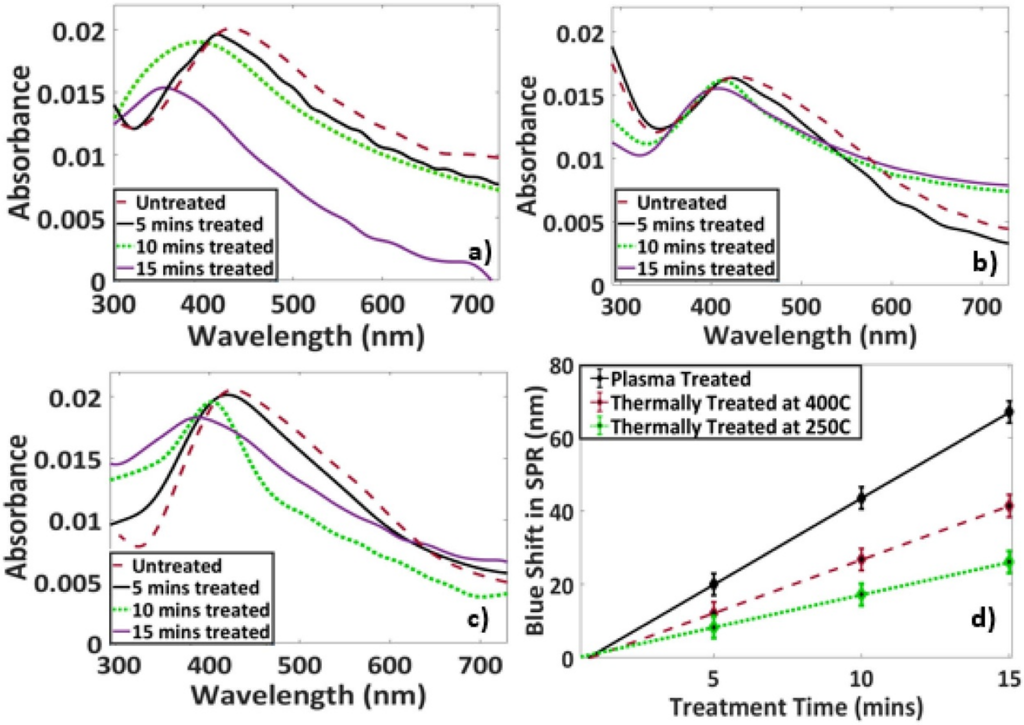

Figure 3. SPR of films (a) plasma-treated, (b) thermally treated at 250 °C, and (c) thermally treated at 400 °C. (d) The blue shift of (a–c) after thermal and plasma treatment.

ratio increased. This led to an increase in the number of scattering electrons at the NP surface, which is responsible for the reduced lifetime of the oscillations and increased spectral width [32].

Our results differ from those of studies that use sintering processes of drop-casted NPs [17,33] because of the deposition technique. After aerosol deposition, the lack of liquid media prohibits NP migration and agglomeration. In addition, the process is independent of the substrate and takes place at a low temperature. Hence, it allows NPs to be processed individually, which contributes to the size reduction and blue shift in the SPR signal. To confirm this explanation [34], we repeated the experiments using drop casting as the deposition method; this led to coalescence and a red shift in the SPR signal, as shown in the supplementary work (available online at stacks.iop.org/NANO/31/365706/mmedia).

3.2. SEM imaging

The Ag NPs were deposited on silicon substrates using the same deposition conditions used for the SPR study. The substrates were then thermally annealed at 400 °C or plasma-treated for 15 min. Figures 4(a)–(c) show the SEM images of the untreated, thermally annealed, and plasma-treated samples, respectively. The size of the NPs was reduced, and the NPs were well dispersed after both treatments.

The SEM images were processed in ImageJ to identify the NP boundaries (figures 4(d)–(f)) and to determine their Feret's diameter (figures 4(g)–(i)). Untreated NPs have an average Feret's diameter of ∼15 nm with the largest particle size of 44 nm because of NP agglomeration during deposition. After thermal annealing, the mean Feret's diameter was reduced to 6 nm, with the diameter of most particles falling in the range of 5–7 nm. Similarly, for the plasma-treated sample, the particle distribution was further narrowed with a mean diameter of 5 nm.

3.3. Surface charge measurements

The zeta potential changed from +25.1 ± 4 mV of the untreated sample to −25.9 ± 6 mV after 15 min of plasma treatment, as shown in figure 5. The magnitude of the zeta potential defines the NP stability due to interparticle electrostatic repulsion. The high magnitude of the untreated Ag NPs is due to the BPEI coating, which imparts positive charge. Similarly, the high magnitude after the treatment (with reversed polarity) ensures the NPs remain stably dispersed. The observed change in the zeta potential and the possible mechanism behind it has been discussed in section 3.5.

3.4. TEM and AFM imaging

Figures 6(a)–(b) show the TEM images of untreated and plasma-treated Ag NP samples prepared on copper grids. The untreated NPs were agglomerated but the plasma-treated NPs were well organized and dispersed. The NP size was reduced after the plasma treatment and a surface oxide formed (figure 6(b)). The diffraction pattern shown in figure 6(a) reveals that the untreated NP film was polycrystalline with various diffraction rings. The diffraction pattern of the NP film tended towards single crystallinity because of the un-piling of NPs as a result of plasma treatment.

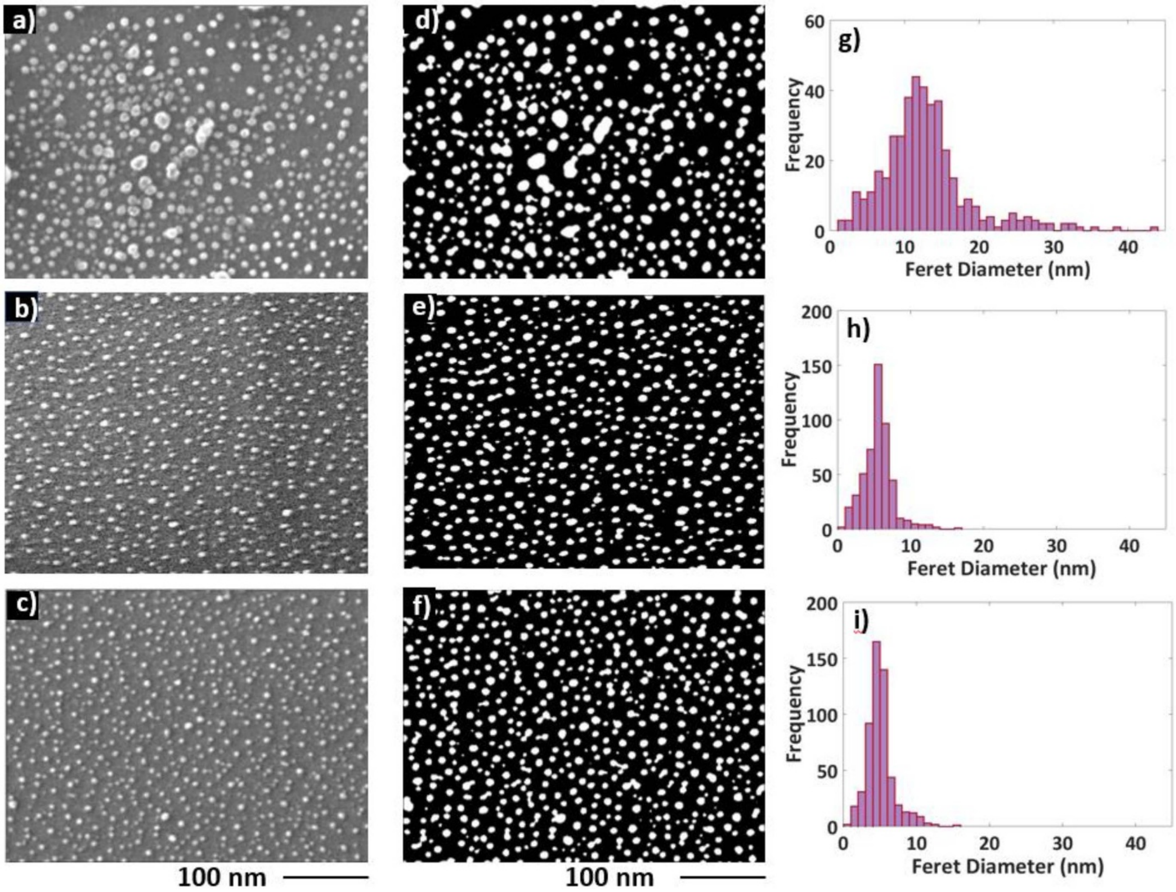

Figure 4. SEM images of the Ag NP films deposited on silicon substrates (a) before treatment, (b) after 15 min of thermal annealing, and (c) after 15 min of plasma treatment. The SEM images were processed in ImageJ to identify the nanoparticle boundaries ((d), (e) and (f)), and Feret's diameter distributions ((g), (h) and (i)) corresponding to untreated, thermally treated, and plasma-treated NPs. The shift in the NP size distribution was attributed to the size reduction after either treatment. The plasma-treated NPs exhibited a more uniform film than the other samples.

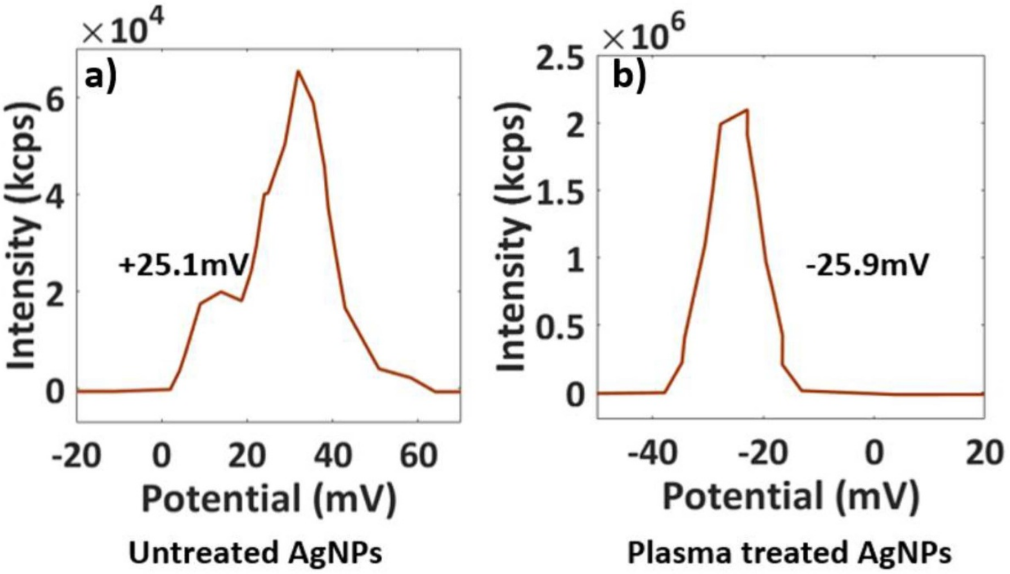

Figure 5. Zeta potential distribution of (a) untreated and (b) plasma-treated (15 min) Ag NPs. The surface charge changes from +25.1 to −25.9 mV after treatment.

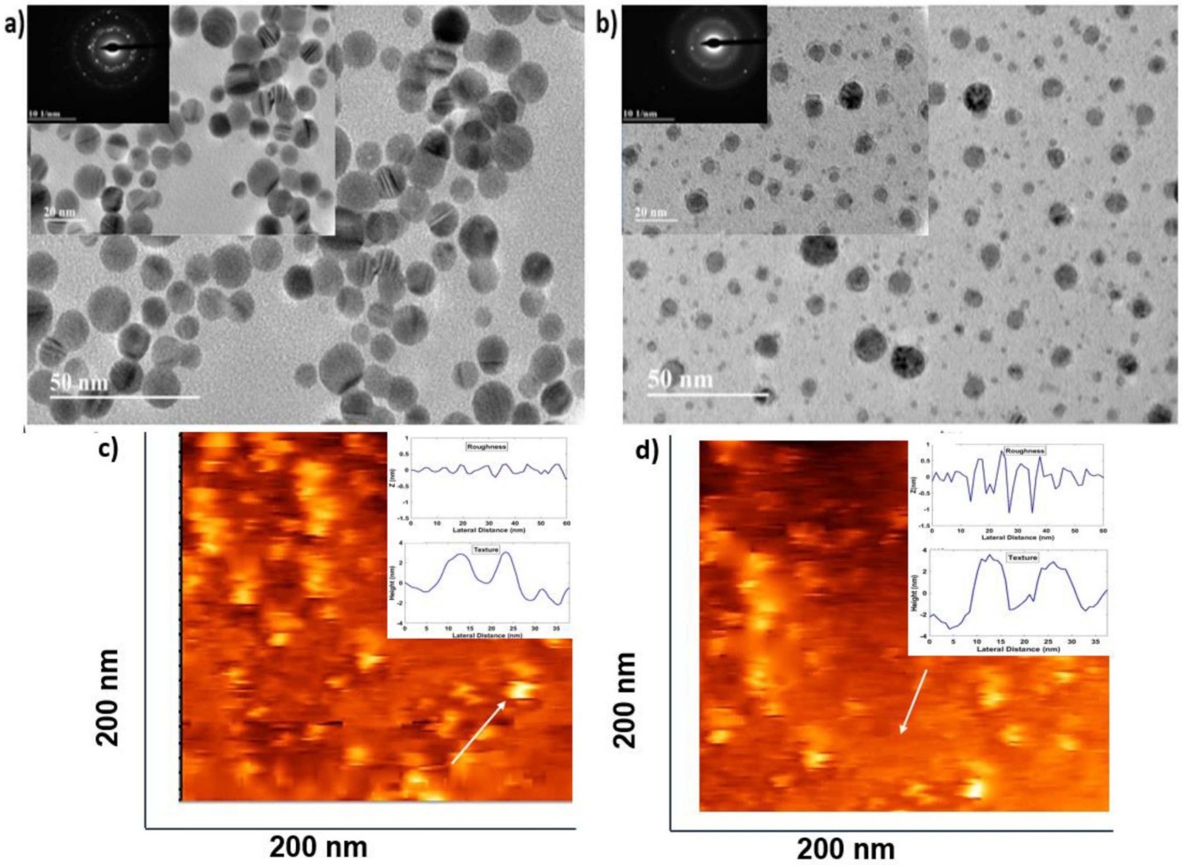

Figure 6. TEM images and diffraction patterns (insets) of (a) untreated and (b) plasma-treated Ag NPs. AFM images of (c) untreated and (d) plasma-treated Ag NP film; the roughness and texture are shown in the insets.

The surface roughness was quantified for untreated and plasma-treated (15 min) Ag NPs, as shown in the inset of figure 6(c). The plots of the roughness of untreated and treated samples show the increase in the amplitude and the number of peaks after treatment for the same projected area. The topology of the selected area (indicated by the white arrow) for the untreated sample is shown in the inset of figure 6(d). The untreated sample shows a smooth topology, and the treated sample shows a rough surface. The mean roughness changed from 1.12 to 1.4 nm, and the route mean square roughness changed from 2.2 to 3.2 nm.

3.5. *Mechanism of plasma-induced reduction in NP size*

Our proposed mechanism of Ag NP surface modification due to the plasma treatment is presented in figure 7. The BPEI coating on the NPs provides electrosteric repulsion between particles and prevents agglomeration [35]. Because the BPEI electrosteric stabilization involves electrostatic and steric bonding between the particle and polymer, NPs acquires a positive surface charge [36] (as confirmed by zeta potential measurement in section 3.3). Negatively charged ions are then adsorbed on the surface of positively charged NPs in the Stern potential region to form an electric double layer (EDL) [37].

We believe that as the thermal annealing process starts, the EDL that is formed around the surface of the NPs breaks and leaves a net positive surface charge. Because the BPEI coating has a flashpoint at 110 °C, the NP–polymer electrosteric bonds are broken by further annealing at 250 and 400 °C [37]. In the case of plasma treatment, the energetic electrons (average energy ∼1 eV) provide enough energy to break the weak bonds between the BPEI polymer and the surface of the NPs [38]. The Raman spectrum in figure 7(b) shows intense peaks at 123.8 and 142.2 cm^{-1} attributed to the vibrational mode of the Ag lattice [39]. These peaks are enhanced after plasma treatment, which validates our hypothesis that the coating is removed from the NP surface during treatment. The Raman spectrum shows an intense band of amine bending at 1600 cm^{-1}, which can be observed after 5 min of plasma treatment owing to the breaking of the amine group of the BPEI coating from the NP surface [40]. The shift of this band to 1555 cm^{-1}, and the bands at 1442 and 1062 cm^{-1} are attributed to the protonation of an amino group of PEI. The Raman peaks at 791 and 885 cm^{-1} are due to vibrations of the ethylene groups present [40]. The band at 942 cm^{-1} was enhanced after plasma treatment up to 15 min, which indicates the breaking of BPEI bonding and removal of the coating from the NP surface. After 15 min, the intensity of this band decreased owing to the formation of the surface oxide layer. The SERS of BPEI is very weak at 532-nm excitation; hence, this excitation wavelength was used to detect R6 G peaks (as shown in section 3.5) to study the structural changes of the surface of the

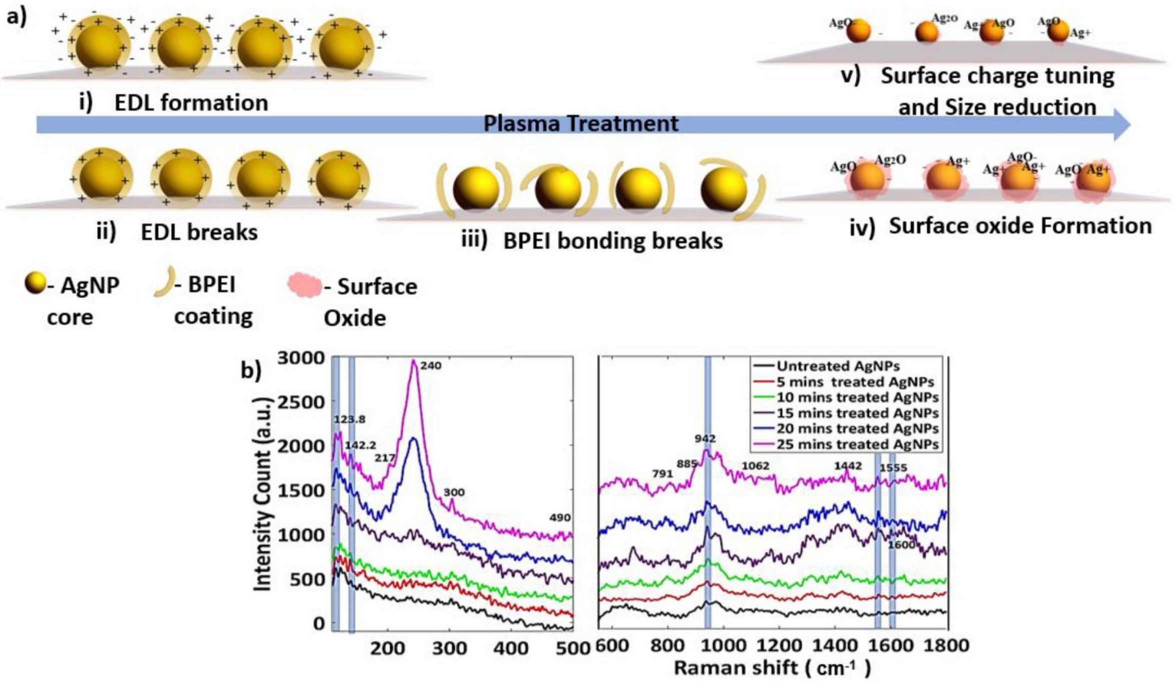

Figure 7. (a) Proposed mechanism by which plasma treatment modifies Ag NP films. The bottom panel (b) is the SERS spectra of the untreated and plasma-treated NPs at 532-nm excitation, which validates the hypothesis that removal of the BPEI coating and subsequent surface oxide formation results in the observed size reduction.

Ag NPs. Further, a new EDL forms owing to the ions and electrons present in the downstream plasma. For the CAP set-up used in this work, the Debye length is ~75 μm [41]. Therefore, the potential developed between the surface and the plasma is confined in the plasma sheath, which is much larger than the EDL formed on the NP surface.

The energy provided by plasma treatment was sufficient to keep the surfaces of the NPs separated by distances equal to the repulsive barrier. The plasma-treated NPs formed an organized NP film on the substrate as they settled during deposition, under attractive Van der Waals forces. Although some positive surface charges on Ag NPs are nullified by electrons, Ag^+ also combines with the reactive oxygen species present in the plasma to form AgO and Ag_2O on the surface. Some Ag^+ ions are also reduced by the plasma electrons. The Raman spectra in figure 7 show a sharp peak at 240 cm^{-1}, which is attributed to the stretching of Ag–O bonds as the reactive oxygen species present in the plasma environment (as shown in section 2.2) react with the surface of the Ag NPs [42]. The peaks at 217, 300, and 490 cm^{-1} are due to O_2 anions in the AgO and AgO_2 lattice, which is evidenced by the formation of an oxide layer on the NP surface [39,43]. The low intensities of all these peaks show the partial oxide formation until 15 min of the treatment. After 15 min, higher intensities were observed, which are attributed to asymmetric oxide layer formation on almost the entire NP surface. The ratio of intensities of the Ag lattice vibrations at 123.8 and 142.2 cm^{-1} to AgO at 240 cm^{-1} increased after 20 min of plasma treatment, indicating a higher coverage of the oxide layer. Hence, changes in morphology and optical properties were observed until 15 min of treatment.

The lower intensity of the SPR absorbance peak after plasma treatment, as shown in figure 3, can also be explained as a consequence of the decrease in the net positive charge on the Ag NP surface after treatment [44]. The reduction in the NP size is also due to the surface oxide layer. The negative charge density developed on the NPs is desorbed when plasma species provide the appropriate activation energy leading to the sublimation of the surface oxide [45]. The minimum energy required to decompose the Ag_2O layer is 1.25 eV and the reduction potential of Ag^+ is 0.8 V [46]. The average electron energy in the downstream plasma is 1 eV (see section 2.2), which is sufficient to remove the BPEI coating, form a surface oxide, change the surface charge, and ultimately reduce the particle size. However, the plasma energy is slightly lower than that required for decomposition of the Ag_2O oxide layer formed after 20 min of treatment, as shown in the Raman spectra in figure 7.

3.6. *SERS characterization of the plasma-treated NP film*

Figures 8(a)–(b) show the SERS signals for R6 G on the untreated sample and after plasma treatment for 3, 5, 10, 15, 20, and 25 min. Prominent R6 G peaks were detected at 612, 772, 930, 1084, 1127, 1187, 1310, 1364, 1419, 1507, 1575, and 1648 cm^{-1} for the untreated and plasma-treated samples. The spectra also show additional peaks at 658, 1084, 1127, 1275, and 1595 cm^{-1} for the plasma-treated samples. The spectra for samples treated from 3 to 15 min showed the sharpest lower-intensity peaks. These peaks were suppressed in the untreated sample. Moreover, the SERS signal at 1364 cm^{-1} after 15 min of treatment was ~120 times

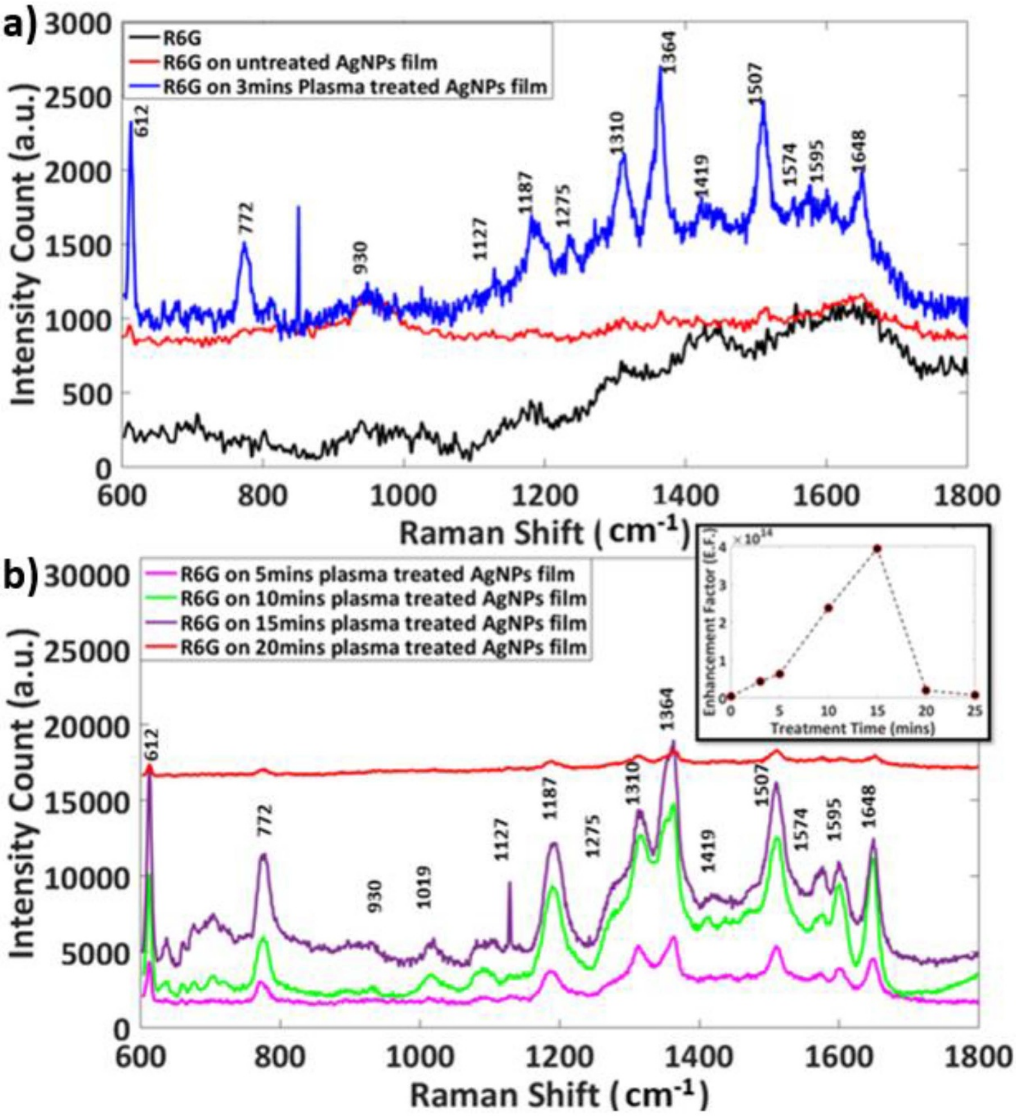

Figure 8. SERS response of R6 G on as-deposited and plasma-treated Ag NP films on a silicon substrate. The R6 G response is enhanced until 15 min of plasma treatment, after which it saturates because of the complete surface coverage of the oxide layer. The inset in (b) shows the enhancement factor of R6 G as a function of treatment time.

higher than that of the untreated film. This shows the promising improvement of SERS performance of plasma-treated Ag NP films.

The uneven redox reaction occurring on the NP surface, leading to the increased surface roughness and hot-spots created at nanogaps [47], also contributed to the SERS enhancement. The untreated NPs agglomerated, resulting in lower SERS enhancement than for the plasma-treated samples [47]. The inset of figure 8(b) shows the change in intensities of the SERS peaks for the untreated and treated samples. The enhancement factor (EF) was calculated for the R6 G peak at 612 cm^{-1} as 7.8×10^{14}, and that of at 1364 cm^{-1} was calculated as 3.4×10^{14} for 15 min of plasma treatment. The EF was reduced after 20 min of treatment because of asymmetric or entire surface oxidation, as described in section 3.5. The enhancement in the Raman peaks of the R6 G signal until 15 min of plasma treatment with a subsequent decay validate the mechanism discussed in section 3.5.

The stability studies of plasma-treated AgNPs SERS substrates have shown stable enhancement until 96 h after the treatment. The results have been added in the supplementary work.

4. Conclusions

We optimized plasma-assisted aerosolized NPs deposition, which resulted in a reduction of NP size and the formation of a well-dispersed film, as confirmed by SPR and SEM. The results obtained for the plasma treatment at room temperature were comparable to those of thermal treatment at elevated temperatures. Thus, this technique can be implemented in areas where thermal treatment and its inherently complex assembly is not desirable for size-controlled NP film deposition.

The plasma-induced redox reaction resulted in morphological changes in the Ag NPs and increased surface roughness, as confirmed through TEM and AFM. The enhancement in the SERS signal highlights the potential of our method to be used to prepare sensitive SERS substrate for biosensing applications. These substrates can be formed at room temperature and on flexible materials, such as polymers, papers, and textiles. Moreover, we demonstrate that this method can be used to tune the surface charge of the Ag NPs. This could be exploited for electrochemical sensing because it increases the activity and affinity towards specific charged molecules. Our work opens new avenues in nanotechnology and will spur further studies into understanding the effects of plasma treatment on NPs.

Acknowledgments

This work is being supported by the NSF Nanosystems Engineering Research Centre for Advanced Self-Powered Systems of Integrated Biosensors and Technologies (ASSIST) under Award Number EEC-1160483 and NSF PFI-TT Award number 1827682.

ORCID iDs

Apurva Sonawane https://orcid.org/0000-0001-6593-3125
Mubarak A Mujawar https://orcid.org/0000-0003-2857-8309
Shekhar Bhansali https://orcid.org/0000-0001-5871-9163

References

[1] Diaz Fernandez Y A, Gschneidtner T A, Wadell C, Fornander L H, Lara Avila S, Langhammer C, Westerlund F and Moth-Poulsen K The conquest of middle-earth: combining top-down and bottom-up nanofabrication for constructing nanoparticle based devices 2014 *Nanoscale* **6** 14605–16

[2] Mosier-Boss P A 2017 Review of SERS substrates for chemical sensing *Nanomater* **7** 6

[3] Lane L A, Qian X and Nie S SERS nanoparticles in medicine: from label-free detection to spectroscopic tagging 2015 *Chem. Rev.* **115** 10489–529

[4] Chan T-Y, Liu T-Y, Wang K-S, Tsai K-T, Chen Z-X, Chang Y-C, Tseng Y-Q, Wang C-H, Wang J-K and Wang Y-L SERS detection of biomolecules by highly sensitive and reproducible raman-enhancing nanoparticle array 2017 *Nanoscale Res. Lett.* **12** 344

[5] Rodriguez-Lorenzo L and Alvarez-Puebla R A 2014 Surface-enhanced raman scattering (SERS) nanoparticle sensors for biochemical and environmental sensing *Nanosensors Chem. Biol. Appl.* 197–230

[6] Wu W, Wu M, Sun Z, Li G, Ma Y, Liu X, Wang X and Chen X 2013 Morphology controllable synthesis of silver nanoparticles: optical properties study and SERS application *J. Alloys Compd.* **579** 117–23

[7] Kim Y-T, Schilling J, Schweizer S L and Wehrspohn R B Morphology dependence on surface-enhanced raman scattering using gold nanorod arrays consisting of agglomerated nanoparticles 2017 *Plasmonics* **12** 203–8

[8] Mogensen K B and Kneipp K Size-dependent shifts of plasmon resonance in silver nanoparticle films using controlled dissolution: monitoring the onset of surface screening effects 2014 *J. Phys. Chem.* C **118** 28075–83

[9] Mohammad Naim N, Abdullah H, Umar A A, Abdul Hamid A and Shaari S 2015 Thermal annealing effect on structural, morphological, and sensor performance of PANI-Ag-Fe based electrochemical E. coli sensor for environmental monitoring *Sci. World J.* **2015** 696521

[10] Pandey P, Kunwar S, Sui M, Li M-Y, Zhang Q and Lee J Effect of annealing temperature on morphological and optical transition of silver nanoparticles on *c* -plane sapphire 2018 *J. Nanosci. Nanotechnol.* **18** 3466–77

[11] Jain P K, Huang X, El-Sayed I H and El-Sayed M A Noble metals on the nanoscale: optical and photothermal properties and some applications in imaging, sensing, biology, and medicine 2008 *Acc. Chem. Res.* **41** 1578–86

[12] Farka Z, Juřík T, Kovář D, Trnková L and Skládal P Nanoparticle-based immunochemical biosensors and assays: recent advances and challenges 2017 *Chem. Rev.* **117** 9973–10042

[13] Garrido C, Weiss-López B E and Campos Vallette M M Surface-enhanced raman scattering activity of negatively charged bio-analytes from a modified silver colloid 2016 *Spectrosc. Lett.* **49** 11–18

[14] Sundaresan V, Monaghan J W and Willets K A Visualizing the effect of partial oxide formation on single silver nanoparticle electrodissolution 2018 *J. Phys. Chem.* C **122** 3138–45

[15] Hong S Selective laser sintering of nanoparticles *Sintering of Functional Materials* Rijeka: InTech 2018

[16] Duan Y, Rani S, Newberg J T and Teplyakov A V Investigation of the influence of oxygen plasma on supported silver nanoparticles 2018 *J. Vac. Sci. Technol.* A **36** 01B101

[17] Okeil S and Schneider J J 2018 Controlling surface morphology and sensitivity of granular and porous silver films for surface-enhanced raman scattering, SERS *Beilstein J. Nanotechnol.* **9** 2813–31

[18] Sonawane A, Mujawar M A and Bhansali S 2019 Atmospheric plasma treatment enhances the biosensing properties of graphene oxide-silver nanoparticle composite *J. Electrochem. Soc.* **166** B3084–B3090

[19] Dey A, Krishnamurthy S, Bowen J, Nordlund D, Meyyappan M and Gandhiraman R P 2018 Plasma jet printing and *in situ* reduction of highly acidic graphene oxide *ACS Nano* **12** 5473–81

[20] Khan T M, Pokle A and Lunney J G 2018 Atmospheric pulsed laser deposition of plasmonic nanoparticle films of silver with flowing gas and flowing atmospheric plasma *Appl. Phys.* A **124** 336

[21] Duque J S, Blandón J S and Riascos H 2017 Localized plasmon resonance in metal nanoparticles using mie theory *J. Phys. Conf. Ser.* **850** 012017

[22] Hoffmann V and Quentmeier A 2011 Glow discharge optical emission spectroscopy (GD-OES) *Surface and Thin Film Analysis* (Weinheim: Wiley) 329–44

[23] Lock E H, Boris D R, Walton S G, Fernsler R F and Sin I L 2010 Optical emission spectroscopy measurements of electron beam-generated plasma in argon, nitrogen and their mixtures In *2010 Abstracts IEEE International Conference on Plasma Science* (Piscataway, NJ: IEEE) 11486036

[24] Sarani A, Nikiforov A Y and Leys C 2010 Atmospheric pressure plasma jet in Ar and Ar/H_2O mixtures: Optical emission spectroscopy and temperature measurements *Phys. Plasmas* **17** 063504

[25] Murbat H, Aadim K A, A-K Hussain A, KhAbdalameer N, Ali Tawfeeq H and Murbat H H Electron temperature and density measurement of plasma jet in atmospheric pressure *Int. J. Nov. Res. Phys. Chem. Math.* **2** 28–32

[26] Seesahai B 2016 *Plasma Temperature Measurements in the Context of Spectral Interference* (University of Central Florida)

[27] Safi A, Tavassoli S H, Cristoforetti G, Legnaioli S, Palleschi V, Rezaei F and Tognoni E 2019 Determination of excitation temperature in laser-induced plasmas using columnar density Saha-Boltzmann plot *J. Adv. Res.* **18** 1–7

[28] Le Ru E C, Blackie E, Meyer M and Etchegoin P G 2007 Surface enhanced raman scattering enhancement factors: a comprehensive study *J. Phys. Chem. C* **111** 13794–803

[29] Qin J, Pan L, Li C, Xia L, Zhou N, Huang Y and Zhang Y 2017 Controlled preparation of Ag nanoparticles on graphene with different amount of defects for surface-enhanced raman scattering *RSC Adv.* **7** 27105–12

[30] Amendola V and Meneghetti M 2009 Size evaluation of gold nanoparticles by UV#vis spectroscopy size evaluation of gold nanoparticles by UV-vis spectroscopy *J. Phys. Chem.* C **113** 4277–85

[31] Haiss W, Nguyen T K T, Aveyard J and Fernig D G 2007 Determination of size and concentration of gold nanoparticles from UV−vis spectra *Anal. Chem.* **79** 4215–21

[32] Garcia M A and García M A 2011 Surface plasmons in metallic nanoparticles: fundamentals and applications surface plasmons in metallic nanoparticles surface plasmons in metallic nanoparticles: fundamentals and applications *Phys. D Appl. Phys.* **44** 283001

[33] King S R, Gentle A R, Cortie M B and McDonagh A M 2018 On the development of optical properties during thermal coarsening of gold nanoparticle composites *J. Phys. Chem.* C **122** 12098–105

[34] Eklöf J, Gschneidtner T, Lara-Avila S, Nygård K and Moth-Poulsen K 2016 Controlling deposition of nanoparticles by tuning surface charge of SiO_2 by surface modifications *RSC Adv.* **6** 104246–53

[35] Zewde B M, Ambaye A B, Stubbs J T and Raghavan D 2017 A review of stabilized silver nanoparticles – synthesis, biological properties, characterization, and potential areas of applications. JSM nanotechnol *Nanomed* **4** 1–14

[36] Signori A M, Santos K, De O, Eising R, Albuquerque B L, Giacomelli F C and Domingos J B 2010 Formation of catalytic silver nanoparticles supported on branched polyethyleneimine derivatives. *Langmuir* **26** 17772–9

[37] Badawy A M E, Luxton T, Silva P, Scheckel R G, Suidan K G and Tolaymat M T 2010 Impact of environmental conditions (PH, ionic strength, and electrolyte type) on the surface charge and aggregation of silver nanoparticles suspensions *Environ. Sci. Technol.* **44** 1260–6

[38] Fritz G, Schädler V, Willenbacher N and Wagner N J 2002 Electrosteric stabilization of colloidal dispersions *Langmuir* **18** 6381–90

[39] Martina I, Wiesinger R, Jembrih-Simbuerger D and Schreiner M 2012 Micro-Raman Characterisation of Silver Corrosion Products: Instrumental Set Up And Reference Database (www.Morana-rtd.com)

[40] Sanchez-Cortes S, Berenguel R M, Madejón A and Pérez-Méndez‡ M 2002 Adsorption of polyethyleneimine on silver nanoparticles and its interaction with a plasmid DNA: a surface-enhanced raman scattering study *Biomacromolecules* **3** 655–60

[41] Grill A 1994 *Cold Plasma in Materials Fabrication : From Fundamentals to Applications* (IEEE Press)

[42] Kora A J and Arunachalam J 2012 Green fabrication of silver nanoparticles by gum tragacanth (*astragalus gummifer*): a dual functional reductant and stabilizer. *J. Nanomater.* **2012** 1–8

[43] Waterhouse G I N, Bowmaker G A and Metson J B 2001 The thermal decomposition of silver (I, III) oxide: a combined XRD, FT-IR and raman spectroscopic study *Phys. Chem. Chem. Phys.* **3** 3838–45

[44] Abbaszadegan A, Ghahramani Y, Gholami A, Hemmateenejad B, Dorostkar S, Nabavizadeh M and Sharghi H 2015 The effect of charge at the surface of silver nanoparticles on antimicrobial activity against gram-positive and gram-negative bacteria: a preliminary study *J. Nanomater.* **2015** 1–8

[45] McVicker J E, Rapp R A and Hirth J P 1975 The sublimation of basal surfaces of zinc oxide *J. Chem. Phys.* **63** 2646–58

[46] L'vov B V 1999 Kinetics and mechanism of thermal decomposition of silver oxide *Thermochim. Acta* **333** 13–19

[47] Li J, Chen C, Jans H, Xu X, Verellen N, Vos I, Okumura Y, Moshchalkov V V, Lagae L and Van Dorpe P 2014 300 Mm wafer-level, ultra-dense arrays of Au-capped nanopillars with sub-10 Nm gaps as reliable SERS substrates. *Nanoscale* **6** 12391–6